

PSFC/JA-03-7

**X-ray Spectroscopy of High n Transitions of He- and Ne-like
Ions in Alcator C-Mod Plasmas**

View metadata, citation and similar papers at core.ac.uk

brought to you by  CORE
provided by DSpace@MIT

J.L. Terry, U.I. Safronova²

March 2003

Plasma Science and Fusion Center
Massachusetts Institute of Technology
Cambridge, MA 02139 USA

¹Lawrence Livermore National Laboratory, Livermore, CA 94550 USA

²Notre Dame University, Notre Dame, IN 46556 USA

This work was supported by the U.S. Department of Energy, Cooperative Grant No. DE-FC02-99ER54512. Reproduction, translation, publication, use and disposal, in whole or in part, by or for the United States government is permitted.

Submitted for publication to *Springer Series Atoms and Plasmas*.

X-ray Spectroscopy of High n Transitions of He- and Ne-like Ions in Alcator C-Mod Plasmas

J. E. Rice, K. B. Fournier[†], E. S. Marmor, J. L. Terry and U. I. Safronova[‡]

Plasma Science and Fusion Center, MIT, Cambridge, MA 02139-4307

[†]*Lawrence Livermore National Laboratory, Livermore, CA 94550, USA*

[‡]*Notre Dame University, Notre Dame, IN 46556*

Abstract

The Rydberg series ($1s^2 - 1snp$) up to $n=14$ of helium-like argon ($Z=18$) has been observed from Alcator C-Mod plasmas using a high resolution x-ray spectrometer array. High n satellites to these lines of the form $1s^22s - 1s2snp$ and $1s^22p - 1s2pnp$ with $3 \leq n \leq 12$ have been recorded. X-ray spectra of $2l - n'l'$ transitions with $3 \leq n \leq 18$ in molybdenum ($Z=42$) and $3 \leq n \leq 12$ in krypton ($Z=36$) and niobium ($Z=41$) from charge states around neon-like have also been measured. Numerous examples of the configuration interaction, which alters the line intensities in some transitions of neon-like ions with nearly degenerate upper levels, have been observed. Accurate wavelengths of all of these transitions ($\pm .5 \text{ m}\text{\AA}$) have been determined by comparison to neighboring reference lines from H- and He-like charge states. Line identifications have been made by comparison to *ab initio* atomic structure calculations, using a fully relativistic, parametric potential code. Measured line intensities have been compared with collisional radiative modeling that includes the contributions from dielectronic recombination and inner shell excitation rates, with good agreement.

I. Introduction

A wide variety of plasma diagnostic applications is available from the measurement of the relatively simple x-ray spectra of He-like ions (Ref.[1] and references therein). The $n=2$ and $n=3$ x-ray spectra from many mid- and high- Z He-like ions have been studied in tokamak plasmas [2-4] and in solar flares [5-6]. The high n Rydberg series of medium Z helium-like ions have been observed from Z -pinches [7,8], laser produced plasmas [9], exploding wires [8], the solar corona [10], tokamaks [11-13] and ion traps [14]. Always associated with x-ray emission from these two electron systems are satellite lines from lithium-like ions. Comparison of observed x-ray spectra with calculated transitions can provide tests of atomic kinetics models and structure calculations for helium- and lithium-like ions. From wavelength measurements, a systematic study of the n and Z dependence of atomic potentials may be undertaken. From the satellite line intensities, the dynamics of level population by dielectronic recombination and inner shell excitation may be addressed.

Satellites to the Ar^{16+} Rydberg series for $n=2$ [15,11], $n=3$ [8,13] and $n=4,5$ [11,12,16] have been examined extensively. Theoretical calculations of $n \geq 3$ satellites for argon (and other elements) are plentiful [12,16-20]. The diagnostic potential of He-like spectra for $n=3$ and higher n transitions has been exhaustively developed [21,22] as well as the use of inner shell excited satellites as a measure of Li-like to He-like ion abundance [23]. For $n \geq 6$ satellites, some wavelengths have been reported [8,11,12,16], and wavelengths and oscillator strengths have been calculated up to $n=7$ [7,8,16], but various wavelength calculations differ from the measured values by 3 mÅ. A comprehensive study of satellites up to $n=12$ in argon and chlorine may be found in Ref.[16]. Observations for Cl^{15+} $n=2$ transitions have been made in Alcator A [24], Alcator C [25], JET [26] and COMPASS-D [26] plasmas, and $n=3$ transitions have been seen in laser produced plasmas [9].

There has also been considerable interest in x-ray transitions from high Z atoms with charge states around the neon-like isosequence, attained in pulsed power [27-29,8], tokamak [30-36] and laser produced [37-39] plasmas. X-ray lasing [40,41] has

been demonstrated in neon-like ions, and a need to understand the kinetics of this system has motivated development of very precise collisional-radiative modeling tools [42]. The identifications of many x-ray lines from neon-like ions allow high resolution experimental data to be used for benchmarking multi-electron atomic structure calculations [43-47,32-34,36]. Collisional radiative modeling of line intensities from neon-, fluorine-, sodium- and magnesium-like ionization states has demonstrated the importance of excitation-autoionization in overall charge state balance in tokamak plasmas [48]. Rates for this process, in conjunction with the latest dielectronic recombination rates [49], have led to a reassessment of the importance of molybdenum radiation in energy balance [50] in tokamak plasmas. Most of the work that has been done previously has been limited to $3 - 3$, $2 - 3$ and $2 - 4$ transitions in the Ne-I iso-electronic sequence and adjacent charge states. Recently, high n lines in neon-like iron have been observed from astrophysical plasmas [51]. High temperature, optically thin tokamak plasmas enable the measurement of many lines originating in transitions from levels having $n \geq 5$; in fact, all of the transitions in the $2p - nd$ series in Mo^{32+} lying under the ionization potential have been measured [33]. The availability of a large number of transitions in several adjacent elements provides the opportunity to study the systematics of configuration interaction (CI) effects [34,36]. Numerous instances of different transitions that are enhanced or suppressed by CI are presented in Ref.[36].

The organization of this paper is as follows. The experimental setup and code description are reviewed in Sections II and III. Observations and code comparisons for the Rydberg series of helium-like Ar^{16+} between $n=3$ and 14, and the high n satellites of Ar^{15+} with $3 \leq n \leq 12$ are presented in Section IV. In Section V, experimental results for high n ground state transitions in Mo ($n \leq 18$) and Kr ($n \leq 12$) are compared with theory, with numerous examples of configuration interaction effects being demonstrated. A summary is given in Section VI.

II. Experiment Description

Most of the x-ray observations described here were obtained from the Alcator C-Mod [52] tokamak. Alcator C-Mod is a compact high field device (minor radius of 21 cm) with all molybdenum plasma facing components, strong shaping capabilities and auxiliary heating by ICRF waves. For the measurements presented here, plasma parameters were in the range of $0.9 \times 10^{20} / \text{m}^3 \leq n_{e0} \leq 3.4 \times 10^{20} / \text{m}^3$ and $900 \text{ eV} \leq T_{e0} \leq 3000 \text{ eV}$. Molybdenum is an intrinsic impurity and argon and krypton were introduced through a piezo-electric valve. An example of argon injection is shown in Fig.1. The 30 ms wide voltage waveform for the piezo valve is shown in the bottom frame, along with the Ar^{16+} x-ray brightness, which peaks after about 200 ms, and stays relatively constant thereafter because of the recycling properties of argon. Also shown in the figure are the electron density and temperature, and the deduced argon density, which is about 3×10^{-4} of the electron density, not enough to perturb the plasma. A laser blow-off impurity injection system [53], which has been used to study impurity transport, was employed to inject palladium, niobium and zirconium. Shown in Fig.2 is the time history of neon-like Nb^{31+} x-ray emission following a niobium injection at 0.5 seconds into an L-mode discharge, when the central electron temperature was 2200 eV and the central electron density was $1.3 \times 10^{20} / \text{m}^3$. The niobium stayed in the plasma for about 100 ms, as shown by the bottom frame of the figure, indicative of anomalously fast impurity transport [54]. This fast L-mode transport, which is comparable to some recombination times, creates a ‘recombining plasma’ at the edge [11].

The x-ray spectra from Alcator C-Mod were recorded by a five chord, independently spatially scannable, high resolution x-ray spectrometer array [55]. Four of these von Hamos type spectrometers had quartz crystals with 2d spacings of 6.687 Å, and wavelength coverage from 2.7 to 4.1 Å, 120 mÅ at a time. The remaining spectrometer had an ammonium dihydrogen phosphate (ADP) crystal with a 2d spacing of 10.640 Å, and a wavelength range from 4.3 to 6.5 Å. Each spectrometer has a resolving power, $\lambda/\Delta\lambda$, of 4000, a 2 cm spatial resolution and a luminosity function of $7 \times 10^{-9} \text{ cm}^2\text{sr}$. Wavelength calibration [30-34,36] has been achieved by determining the instrumental dispersions in reference to H- and He-like argon,

chlorine and sulphur lines. The $2l - 3l'$ spectra of krypton (from Alcator C) were obtained with a von Hamos type spectrometer equipped with a pentaerythritol (PET) crystal ($2d = 8.742 \text{ \AA}$), and with wavelength coverage between 6 and 8 \AA . The active area of the position sensitive proportional counter detector was large (12 cm), which allowed for up to 400 m \AA coverage in one wavelength setting, but non-uniformities along the length of the Be entrance window led to sensitivity variations, so some line ratios from opposite ends of the detector may be up to 25% off.

III. Calculation of Energy Levels, Oscillator Strengths and Line Intensities

Ab initio atomic structure calculations for the lithium-, helium- and hydrogen-like isosequences of S, Cl and Ar ($Z=16, 17$ and 18) with $2 \leq n \leq 14$, and the aluminum- through oxygen-like isosequences (ground states $2p^6 3s^2 3p$ to $2s^2 2p^4$, respectively) of Kr ($Z=36$), Mo ($Z=42$), Nb ($Z=41$), Zr ($Z=40$) and Pd ($Z=46$) have been generated using the HULLAC package. HULLAC includes ANGLAR, which uses the graphical angular recoupling program NJGRAF [56] to generate fine structure levels in a jj-coupling scheme for a set of user-specified electron configurations. HULLAC then generates atomic wavefunctions using the fully relativistic, parametric potential code RELAC [57,58], which calculates the full multi-configuration, intermediate coupled level energies and radiative transition rates. RELAC also computes semi-relativistic autoionization transition rates [59] to the ground and excited levels of an adjacent ion. The CROSS [60] suite of codes in the HULLAC package uses a factorization theorem to compute the distorted wave approximation electron-impact excitation rates between all levels of each charge state mentioned above. This includes levels formed by exciting valence shell electrons as well as deeply bound inner shell electrons.

Energy levels and transition probabilities for helium- and lithium-like ions have also been calculated by using the Z-expansion method (MZ code). The energy

matrix is constructed in an LSJ coupling scheme and relativistic corrections are included within the framework of the Breit-Pauli operator using a perturbation approach. The MZ method uses hydrogenic wavefunctions. However, the calculation energies and other characteristics by this method are greatly improved by using many-body perturbation theory to include the Coulomb interaction between electrons as well as relativistic corrections. The Z-expansion method has been described in detail in Refs.[61,62].

IV. He-like and Neighboring Ions

Shown in Fig.3 are x-ray spectra in the vicinity of the first three resonance lines, w_2 ($1s^2 \ ^1S_0 - 1s2p \ ^1P_1$), w_3 ($1s^2 \ ^1S_0 - 1s3p \ ^1P_1$) and w_4 ($1s^2 \ ^1S_0 - 1s4p \ ^1P_1$) in Ar^{16+} . In the $n=2$ spectrum, the forbidden line, z ($1s^2 \ ^1S_0 - 1s2p \ ^3S_1$), and the intercombination lines, x ($1s^2 \ ^1S_0 - 1s2p \ ^3P_2$) and y_2 ($1s^2 \ ^1S_0 - 1s2p \ ^3P_1$) are prominent. Also apparent are the $n=2$ dielectronic satellites k and j , the $n=2$ inner shell satellites q , r , s and t , and the satellites with $n=3$ and $n=4$ spectators, all from lithium-like argon. (See Ref.[11] for the wavelengths and line designations.) For the $n=3$ spectrum, w_3 is dominant, the intercombination line, y_3 ($1s^2 \ ^1S_0 - 1s3p \ ^3P_1$), is greatly reduced in relative magnitude and wavelength (the excitation rates for x_3 and z_3 are miniscule so they are not seen) and the satellites have formed four unresolved features. (See Refs.[11,13,16] for the wavelengths and line designations.) The upper levels of these satellites are the same as for the unresolved satellites marked 3 in the $n=2$ spectrum; in this case the $n=3$ electron makes the transition with the $n=2$ electron as the spectator, whereas for the satellites marked 3 in the $n=2$ spectrum, the $n=2$ electron makes the transition while the $n=3$ electron is the spectator. For the $n=4$ spectrum, w_4 dominates and the satellites have blended to form three unresolved groups: A_4 is related to k and j in the $n=2$ spectrum, B_4 to q and r , and C_4 to s and t . (See Table 6 of Ref.[16] for the wavelengths and line designations of these satellite groups.) The upper levels of these transitions are the

same as for the shoulder marked 4 in the n=2 spectrum. Presented in Fig.4 is an expanded view of the n=4 satellite groups, showing the individual constituents (see Table 6 of Ref.[16]). The relative intensities of these lines are in good agreement with the calculations.

Spectra of w_4 and satellites for plasmas with different central electron temperatures [16] are shown in Fig.5. As the temperature decreases, the intensities of the satellite groups (relative to w_4) increase; in the bottom frame with an electron temperature of less than 1000 eV (from an off-axis view), the satellite group A_4 is nearly as bright as the resonance line. Similar observations were made from Alcator C [11], from radial profile measurements; in fact near the recombining plasma periphery, the satellite group A_5 was actually brighter than w_5 . Also shown in Fig.5 are the corresponding synthetic spectra, generated as described in Ref.[16], which have been normalized to w_4 . The relative intensities of the satellites A_4 , B_4 and C_4 (and A_5) are well reproduced for these three different electron temperature plasmas, supporting the dielectronic recombination and inner shell excitation rates. (A strong Mo^{32+} 6d-2p line [33] at 3230.1 mÅ is visible in these spectra, see next section.)

Shown in Fig.6 is a spectrum from argon including w_4 , w_5 and w_6 from Ar^{16+} , Ly_β from Ar^{17+} and the satellite groups A_5 - A_{12} , B_5 - B_8 and C_5 - C_7 , in an overlapping ‘triplet’ pattern. Plasma parameters for the discharge from which this spectrum was obtained were $n_{e0} = 1.3 \times 10^{20}/\text{m}^3$ and $T_{e0} = 1550$ eV. A synthetic spectrum is shown in the bottom frame, and the agreement is quite good. The transition designations, calculated wavelengths, satellite capture energies, oscillator strengths/satellite intensity factors and inner shell excitation rates (evaluated at 2000 eV) for Ar^{15+} satellites between n=4 and n=12 may be found in Tables 6-10 of Ref.[16]. The measured wavelength differences between the resonance lines, w_n , and the satellite groups A_n , B_n and C_n , as a function of n for argon are shown in Fig.7. Also shown are the theoretical values (curves), from the calculated wavelengths of Tables 6-10 of Ref.[16]; the solid lines are from the MZ wavelengths and the dotted lines represent the wavelengths from RELAC. The agreement between

the observed wavelengths and those calculated from MZ is excellent. This figure may be compared to Fig.3 in Ref.[12].

Spectra near the Ar^{16+} Rydberg series limit [11] are shown in Fig.8. The top spectrum was taken along the central chord of a plasma with $n_{e0} = 0.9 \times 10^{20}/\text{m}^3$ and $T_{e0} = 2600$ eV. The resonance lines from w_6 to w_{14} are clearly resolved, and there is a region of enhanced brightness from w_{15} up to the series limit at $3008.8 \text{ m}\text{\AA}$, presumably due to unresolved lines. Along this chord, most of the line emission is from the plasma center where electron impact excitation is the dominant mechanism for populating the upper levels. Ar^{17+} Ly_γ near $2987.4 \text{ m}\text{\AA}$ is also prominent. The corresponding spectrum from an identical plasma, but taken along a chord viewing through $r/a = 0.67$ (away from the X-point), where the electron temperature was 1100 eV and the electron density was $0.8 \times 10^{20}/\text{m}^3$, is shown in the middle frame of Fig.8. The lines are greatly reduced in intensity and the widths are very narrow due to the lower ion temperature. The intensities of w_9 and w_{10} are enhanced relative to the trend of decreasing intensity with increasing n number, which is due to population by charge exchange recombination with intrinsic neutral deuterium in the ground state, near the plasma edge [63,11]. Emission from the very high n levels ($n > 25$) is also visible just on the long wavelength side of series limit. Along this chord, however, the lines w_{11} through w_{14} are not visible. The viewing chord of the middle spectrum was 18.5 cm above the mid-plane in a discharge with a lower X-point. The continuum at wavelengths shorter than the limit is greater than the continuum level between the resonance lines, and is due to radiative recombination [11]. The spectrum shown in the bottom frame is from a somewhat similar plasma, from a chord viewing through $r/a = 0.62$, but 19.7 cm below the mid-plane, for a lower X-point discharge. In this case w_{10} is enhanced relative to the other w_n lines (due to population by charge exchange with intrinsic neutral deuterium in the ground state) and the feature on the long wavelength side of the limit is now dominant. This feature is from n numbers between 30 and 40 , and is due to charge exchange between hydrogenlike argon and intrinsic neutral deuterium in the $n=3$ and $n=4$ excited states [63,11].

V. Ne-like and Neighboring Ions

Shown in Fig.9 is the 2 – 3 spectrum of neon-like krypton (Kr^{26+}), with satellites [36]; previous observations can be found in Refs. [28,8,37,38]. This is a composite spectrum obtained by scanning in wavelength during a sequence of reproducible Alcator C discharges [36], with a peak electron density of $2.6 \times 10^{20}/\text{m}^3$ and a peak electron temperature of 1450 eV. The spectrum is dominated by the neonlike electric-dipole transitions 3C ($2p_- - 3d_-$ or $2p^6 - (2p^5)_{\frac{1}{2}}3d_{\frac{3}{2}}$) and 3D ($2p_+ - 3d_+$ or $2p^6 - (2p^5)_{\frac{3}{2}}3d_{\frac{5}{2}}$). (The standard notation for Ne-like transitions [65] is used.) The 3F and 3G ($2p_{\mp} - 3s_+$) transitions, including the magnetic quadrupole line (M2, $2p_+ - 3s_+$, $\Delta J=2$) at 7519.2 mÅ, are also intense. Transitions with a 2s hole (3A, $2s - 3p_+$ and 3B, $2s - 3p_-$) are bright, including the electric quadrupole $2s - 2d_+$ line at 6103.8 mÅ. Also apparent are F-, Na- and Mg-like satellites. This composite spectrum is comprised of 6 individual spectra from different discharges, and considering non-uniformities along the detector (as mentioned above), the relative intensities of lines separated by more than 150 mÅ have a 25% uncertainty. Shown in the bottom of Fig.9 is a synthetic spectrum, which is in good qualitative agreement. Transition designations, experimental and theoretical wavelengths and calculated oscillator strengths for all of these lines are presented in Tables I-IV of Ref.[36]. Most observed transitions are within 3 mÅ of the calculated wavelengths, or about 0.04%. The synthetic spectrum was computed for $T_e = 1600$ eV and $n_e = 1.0 \times 10^{20}/\text{m}^3$.

Moving to higher n transitions, shown in Fig.10 are $\Delta n=2$ spectra, with the upper levels in $n=4$, for the neon-like ions Mo^{32+} and Kr^{26+} . The 4D line [33,48] dominates the molybdenum spectrum, and similar transitions from the Na- and F-like charge states are prominent. (See Tables in Ref.[33] for wavelengths and transition designations.) Radial brightness profiles [48] of the five intense $n=4$ molybdenum lines (F-like 3.6149, Ne-like 4C 3.6261, Na-like 3.6710, Ne-like 4D 3.7398 and Na-like 3.7857 Å), obtained during a series of several similar shots, are shown in Fig. 11. The Mo^{32+} profiles (Xs, 4D and plus signs, 4C) dominate

over the inner half of the plasma. The Mo^{31+} profile shapes (red squares and diamonds) are broader, and the Mo^{33+} profile (purple asterisks) is narrower than the Mo^{32+} profiles. Also shown in the top frame of the figure are the calculated brightness profiles (curves) for the five lines, using the charge state density profiles of Fig.4a, Ref.[48], which includes the effects of excitation-autoionization. All of the profile shapes and the relative intensities are well matched by the calculations. This agreement indicates that the combination of the electron temperature and density profiles, the transport coefficients and the excitation, ionization and recombination rates is well characterized for these ionization states over the inner 10 cm. In this region the electron temperature and density profiles and transport coefficients are independently measured and well known. The match in the top frame of Fig. 11 is taken as evidence in support of the charge profiles shown in Fig. 4a of Ref.[48]. The brightness profiles calculated from the charge state profiles of Fig. 4b of Ref.[48] (i.e. those without inclusion of excitation-autoionization) are shown in the bottom frame of Fig. 11, along with the measured profiles. Both the profile shapes and the relative intensities do not represent the data, demonstrating the importance of excitation-autoionization in the overall ionization rate and the sensitivity of this comparison.

Shown in the bottom of Fig.10 are the 4D ($2p_+ - 4d_+$) and 4C ($2p_- - 4d_-$) lines of Kr^{26+} at 5396.4 and 5278.7 mÅ, respectively, along with neighboring satellites and the neonlike 4F ($2p_- - 4s_+$) line at 5407.3 mÅ. Central parameters for the plasma from which this spectrum was obtained were $T_e = 1150$ eV and $n_e = 1.6 \times 10^{20}/\text{m}^3$. These transitions have been studied extensively in molybdenum [33,48]. Also shown is a synthetic spectrum, which is in good agreement with the observations, although there is a ~ -10 mÅ shift of the calculated wavelength for the magnesiumlike $2p_- - 4d_-$ transition at 5436.6 mÅ. The 4F transition at 5407.3 mÅ is readily noticeable, having about 10% of the intensity of the 4D transition; the 4F line in Mo^{32+} at 3705.6 mÅ was too weak to be reported in Ref. [33], but can be seen in the top of Fig.10, with about 1% of the intensity of 4D. The reason the 4F line is so intense in Kr^{26+} is because of its close proximity to the 4D line; the

upper levels are separated by only 4.6 eV, and significant configuration interaction results that transfers strength from 4D to 4F [36]. The energy level diagrams for $n = 4$ transitions in neonlike molybdenum and krypton are shown in Fig.12. As can be seen, the upper levels for the 4D and 4F transitions in Kr^{26+} are very close, within 4.6 eV, while in Mo^{32+} these levels are 31 eV apart, too far away for any significant configuration interaction.

This phenomenon has been seen between the 7D and 6C levels in Mo^{32+} [33,34,36,66], but in contrast here, the *shorter* wavelength line is the beneficiary of the enhanced intensity. This effect is summarized in Fig.13, top frame, where the calculated oscillator strengths of the 6D ($2p^6 - (2p^5)_{\frac{3}{2}}6d_{\frac{5}{2}}$), the 6C ($2p^6 - (2p^5)_{\frac{1}{2}}6d_{\frac{3}{2}}$), the 7D ($2p^6 - (2p^5)_{\frac{3}{2}}7d_{\frac{5}{2}}$) and the 7C ($2p^6 - (2p^5)_{\frac{1}{2}}7d_{\frac{3}{2}}$) lines are plotted as a function of atomic number. The oscillator strengths of the 6D and 7C lines are relatively insensitive to atomic number. The magnitude of the configuration interaction between the 6C and 7D levels is quite apparent; as the atomic number increases from Y to Mo, the g^*f value of the 7D line increases while the value of the 6C line decreases. At technetium ($Z=43$), this effect dramatically switches; for Tc and higher Z elements, the 6C line is at shorter wavelength and the 7D line is the *weaker* of the two. The wavelength differences between the two levels is shown in Fig.13 in the bottom frame. The brightness ratios for these lines as a function of level separation are shown in Fig.14, which is similar to Fig.5 of Ref. [66], but with the inclusion of the krypton points [36]. The agreement between experiment and theory is quite good; it would certainly be gratifying to verify that this effect changes sign in Tc or in Ru. It is noteworthy that in the case of the $2p - nd$ configuration interaction, as in Figs.13 and 14, the ‘beneficiary’ of the enhanced intensity is on the short wavelength side (higher energy side) whereas in the case of $2p - ns$ level enhancement, Fig.10, the ‘beneficiaries’ are on the long wavelength side (lower energy side) of the ‘donor’ transition.

Moving to even higher n transitions, shown in Fig.15 is a spectrum [33] from 2.9 to 3.0 Å, obtained from a series of identical discharges with $n_{e0} = 1.7 \times 10^{20}/\text{m}^3$

and $T_{e0} = 2300$ eV. The nD ($2p_{\frac{3}{2}} - nd_{\frac{5}{2}}$) series (red) up to $n = 18$ and the nC ($2p_{\frac{1}{2}} - nd_{\frac{3}{2}}$) series with $8 \leq n \leq 12$ (green) are clearly resolvable. Above $n = 18$, the lines of the nD series blend together, up to the series limit at 2914.78 mÅ. Also shown are two Ar^{17+} lines used for the wavelength calibration, and a strong F-like Mo^{33+} line at 2929.9 mÅ. At the bottom of the figure are calculated lines from Mo^{32+} (solid), Mo^{33+} (dashed) and Ar^{17+} (dotted). Also visible are the Mo^{32+} 2s-6p and 2s-7p doublets at 2983 and 2903 mÅ, respectively.

Spectra [34] including the nD series limit at 2914.78 mÅ, and the nC series limit at 2841.44 mÅ in Mo^{32+} are shown in Fig.16. The wavelength calibration for these spectra was obtained from the high n series of hydrogen-like Ar^{17+} , transitions from 1s-5p to 1s-10p, with wavelengths of 2917.50 , 2881.04 , 2859.38 , 2845.51 , 2836.07 and 2829.36 mÅ [67]. The calculated nC series in Mo^{32+} [33] with n between 10 and 19 is shown by the thick solid green lines, and the 2s-7p and 2s-8p transitions are shown as the thin solid purple lines. This region of the spectrum is complicated by the presence of many Mo^{33+} transitions, shown as dashed lines. Clearly identified in the top spectrum are the Mo^{32+} 10C line at 2941.0 mÅ, the Mo^{32+} 2s-7p and 2s-8p lines at 2902.1 and 2853.0 mÅ, respectively (see Table II, Ref.[34]), the Mo^{33+} 2p-7d lines at 2935.8 mÅ, and the Mo^{33+} 2p-9d lines at 2930.2 mÅ and 2849.1 mÅ. Clearly missing from this spectrum are the transitions from the Mo^{32+} nC series with $n = 13, 14, 17, 18$ and 19 , which were seen in the nD series. The $n = 11, 12, 15$ and 16 lines have nearby transitions from Mo^{33+} , so the line identifications are ambiguous. The top spectrum of Fig.16 was from a plasma with an electron temperature of 3.4 keV and an electron density of $7.7 \times 10^{19}/\text{m}^3$. At this temperature, Mo^{33+} is the dominant ionization state [68], so the presence of strong fluorine-like lines is expected. In contrast, shown in the bottom of Fig.16 is a spectrum taken from a plasma with $T_e = 2.1$ keV and $n_e = 8.8 \times 10^{19}/\text{m}^3$, where Mo^{32+} is the dominant charge state. In this spectrum, all of the Mo^{33+} lines have dropped in intensity, which suggests that the line at 2883.7 mÅ might be due to 2p-8d Mo^{33+} transitions, and the lines at 2922.8 , 2910.2 and 2878.6 mÅ, respectively, are the 11C, 12C and 16C transitions. The nC transitions with $n \geq 13$ (with the possible exception of 16C)

are missing from the spectra of Fig.16 because the upper states of these transitions lie above the ionization limit of the nD at 2914.78 mÅ, and the branching ratios towards autoionization is greater than 0.9 in every case [34].

VI. Conclusions

The high n Rydberg series of helium-like Ar¹⁶⁺ has been resolved up to n=14 in Alcator C-Mod plasmas, and the associated lithium-like satellites up to n=12 have also been seen. Comparison of observed satellite wavelengths has been made with calculations from two different atomic structure codes, RELAC and MZ, and there is good agreement in general. The calculated intensities of the satellite groups relative to the resonance lines are also in good agreement with the observed line brightnesses, verifying the dielectronic recombination and inner shell excitation rates.

2 – 3 transitions in neon-like Kr has been observed from Alcator C plasmas, in addition to associated fluorine-, sodium- and magnesium-like satellites. Accurate wavelengths have been determined in reference to nearby calibration lines from hydrogen- and helium-like ions. Measured wavelengths and line intensities have been compared with atomic structure calculations and collisional radiative modeling from the RELAC code, with very good overall agreement. High n transitions (up to n=18) in neon-like molybdenum and (up to n=12) in neon-like krypton have also been recorded. Radial profiles of 2p-4d transitions of Na-, Ne- and F-like molybdenum demonstrate the importance of excitation-autoionization in overall charge state balance. Configuration interaction effects in certain neon-like line intensities have been observed, for transitions with nearly degenerate upper levels; comparison of observed line intensities with theory is excellent.

VII. Acknowledgements

The authors would like to thank J. Irby for electron density measurements, A. Hubbard for electron temperature measurements and the Alcator C-Mod operations

groups for expert running of the tokamak. Work supported at MIT by DoE Cooperative Agreement No. DE-FC02-99ER54512. This work was performed under the auspices of the U.S. Department of Energy by the University of California Lawrence Livermore National Laboratory under contract No. W-7405-Eng-48.

References

- [1] J.E.Rice et al., Fusion Eng. Des. **34** and **35**, 159 (1997)
- [2] TFR Group, J. Dubau and M. L. Loulergue, J. Phys. B: At. Mol. Phys. **15**, 1007 (1981).
- [3] M. L. Apicella, R. Bartiromo, F. Bombarda and R. Giannella, Phys. Lett. **98A**, 174 (1983).
- [4] M. Bitter, K. W. Hill, M. Zarnstorff, S. von Goeler, R. Hulse, K. M. Young, L. C. Johnson, N. R. Sauthoff, S. Secnic, M. Tavernier, F. Bely-Dubau, P. Faucher, M. Cornille and J. Dabau, Phys. Rev. A **32**, 3011 (1985).
- [5] C. P. Bhalla, A. N. Gabriel and L. P. Presnyakov, Mon. Not. R. Astron. Soc. **172**, 359 (1975).
- [6] P. Beiersdörfer, R. Philips, V. I. Jacobs, K. W. Hill, M. Bitter, S. von Goeler and S. M. Kahn, Astrophys. J. **409**, 846 (1993).
- [7] N.J.Peacock et al., J. Phys. B **2**, 798 (1969)
- [8] P.G.Burkhalter et al., J. Appl. Phys. **50**, 4532 (1979)
- [9] V.A.Boiko et al., J. Phys. B **10**, 3387 (1977)
- [10] J.F.Seely and U.Feldman, Phys. Rev. Lett. **54**, 1016 (1985)
- [11] J.E.Rice, E.S.Marmar, E.Källne and J.Källne, Phys. Rev. A **35**, 3033 (1987)
- [12] E.Källne et al., Phys. Rev. A **38**, 2056 (1988)
- [13] P.Beiersdörfer et al., Phys. Rev. E **52**, 1980 (1995)
- [14] A.J.Smith et al., Phys. Rev. A **54**, 462 (1996)
- [15] E.Källne et al., Phys. Rev. Lett. **49**, 330 (1982)
- [16] J.E. Rice et al., New J. Phys. **1**, 19 (1999).
- [17] L.A.Vainshtein and U.I.Safronova, At. Data Nucl. Data Tables **25**, 311 (1980)
- [18] C.P.Bhalla and T.W.Tunnell, J. Quant. Spectrosc. Radiat. Transfer **32**, 141 (1984)
- [19] M.H.Chen, At. Data Nucl. Data Tables **34**, 301 (1986)
- [20] J.Nilsen, At. Data Nucl. Data Tables **38**, 339 (1988)

- [21] F. Bely-Dubau, A. H. Gabriel and S. Volonté, Mon. Not. R. Astr. Soc. **186**, 405 (1979).
- [22] F. Bely-Dubau, A. H. Gabriel and S. Volonté, Mon. Not. R. Astr. Soc. **189**, 801 (1979).
- [23] F. Bely-Dubau, J. Dubau, P. Faucher and A. H. Gabriel, Mon. Not. R. Astr. Soc. **198**, 239 (1982).
- [24] J.E.Rice et al., Phys. Rev. A **22**, 310 (1980)
- [25] E.Källne, J.Källne, E.S.Marmar and J.E.Rice, Phys. Scr. **31**, 551 (1985)
- [26] I.H.Coffey et al., in *UV and X-ray Spectroscopy of Astrophysical and Laboratory Plasmas* Frontiers Science Series 15 (Universal Academy Press, Tokyo, 1996, Editors: K.Yamashita and T.Watanabe) p.431
- [27] P. G. Burkhalter et al., Phys. Rev. A **18**, 718 (1978).
- [28] H. Gordon, M.G. Hobby, N.J. Peacock and R.D. Cowan, J. Phys. B **12**, 881 (1979).
- [29] E.V. Aglitskii et al., Physica Scripta **40**, 601 (1989).
- [30] E. Källne, J. Källne and R.D. Cowan, Phys. Rev. A **27**, 2682 (1983).
- [31] P.Beiersdörfer et al., Phys. Rev. A **34**, 1297 (1986)
- [32] P. Beiersdörfer et al., Phys. Rev. A **37**, 4153 (1988).
- [33] J.E.Rice et al., Phys Rev A **51**, 3551 (1995)
- [34] J.E.Rice et al., Phys Rev A **53**, 3953 (1996)
- [35] D. Pacella et al., Phys. Rev. E **61**, 5701 (2000).
- [36] J. E. Rice et al., J. Phys. B **33**, 5435 (2000).
- [37] S. Ya. Khakhalin et al., Phys. Scripta **50**, 106 (1994).
- [38] S. Ya. Khakhalin et al., JETP **78**, 633 (1994).
- [39] S. Ya. Khakhalin et al., J. Opt. Soc. Am. B **12**, 1203 (1995).
- [40] M.D. Rosen et al., Phys. Rev. Lett., **54**, 106 (1985).
- [41] D.L. Matthews et al., Phys. Rev. Lett., **54**, 110 (1985).
- [42] A.L. Osterheld et al., J. Quant. Spectrosc. Radiat. Transfer, **51**, No. 1/2, 263 (1994).

- [43] P. Beiersdörfer, M.H. Chen, R.E. Marrs and M. Levine, Phys. Rev. A **41**, 3453 (1990).
- [44] G.A. Chandler, M.H. Chen, D.D. Dietrich, P.O. Egan, K.P. Ziock, P.H. Mokler, S. Reusch and D.H.H. Hoffmann, Phys. Rev. A, **39**, 565 (1989).
- [45] D.D. Dietrich, G.A. Chandler, P.O. Egan, K.P. Ziock, P.H. Mokler, S. Reusch and D.H.H. Hoffmann, Nucl. Instrum. Methods B, **24/25**, 301 (1987).
- [46] E. Avgoustoglou, W.R. Johnson, Z.W. Liu and J. Sapirstein, Phys. Rev. A **51**, 1196 (1995).
- [47] W.R. Johnson, J. Sapirstein and K.T. Cheng, Phys. Rev. A **51**, 297 (1995).
- [48] J.E. Rice et al., J. Phys. B: At. Mol. Phys. **29**, 2191 (1996).
- [49] K.B. Fournier et al., Phys. Rev. A **54**, 3870 (1996).
- [50] K.B. Fournier, D. Pacella, M.J. May, M. Finkenthal and W.H. Goldstein, Nucl. Fusion **37**, 825 (1997). (corrigendum Nucl. Fusion **38**, 639 (1998).)
- [51] G.V. Brown et al., Ap. J. **502**, 1015 (1998).
- [52] I.H.Hutchinson et al., Phys. Plasmas **1**, 1511 (1994)
- [53] M.A.Graf et al., Rev. Sci. Instrum. **66**, 636 (1995).
- [54] J.E.Rice et al., Phys. Plasmas **4**, 1605 (1997)
- [55] J.E.Rice and E.S.Marmar, Rev. Sci. Instrum. **61**, 2753 (1990)
- [56] Bar-Shalom, A. and Klapisch, M., Computer Phys. Comm. **50**, 375 (1988)
- [57] M.Klapisch, Comput. Phys. Commun. **2**, 239 (1971)
- [58] M.Klapisch, J.L.Schwob, B.S.Fraenkel and J.Oreg, J. Opt. Soc. Am. **67**, 148 (1977)
- [59] Oreg, J., Goldstein, W. H., Klapisch, M. and Bar-Shalom, A., Phys. Rev. A **44**, 1750 (1991)
- [60] Bar-Shalom, A., Klapisch, M. and Oreg, J., Phys. Rev. A **38**, 1773 (1988)
- [61] L.A.Vainshtein and U.I.Safronova, Physica Scripta **31**, 519 (1985)
- [62] U.I.Safronova and J.Nilsen, J. Quant. Spectrosc. Radiat. Transfer **51**, 853 (1994)
- [63] J.E.Rice et al., Phys. Rev. Lett. **56**, 50 (1986)
- [64] J.E.Rice et al., Rev. Sci. Instrum. **66**, 752 (1995)

- [65] J. H. Parkinson, *Astron. & Astrophys.* **24**, 215 (1973).
- [66] J. E. Rice, K. B. Fournier, J. L. Terry, M. Finkenthal, E. S. Marmar, W. H. Goldstein and U.I.Safronova, ‘2l - nl’ X-ray Transitions from Neonlike Charge States of the Row 5 Metals with $39 \leq Z \leq 46$ ’, Proceedings of the 10th Topical Conference on Atomic Processes in Plasmas, San Francisco, CA, January 1996, AIP Press Conference Proceedings 381, Woodbury, NY, pp.11-20 (1996).
- [67] P.J. Mohr, *Phys. Rev. A*, **26**, 2338 (1982) and references 1, 2 and 3 therein.
- [68] K.B. Fournier et al., *Phys. Rev. E* **53**, 1084 (1996).

Figure Captions

Fig. 1 Argon injection via a piezo-electric valve, with the opening voltage waveform shown (green) in the bottom frame along with the Ar^{16+} x-ray brightness (red) time history. The electron density and temperature, along with the argon density are shown.

Fig. 2 Electron temperature, density and Nb^{31+} x-ray brightness time histories for an L-mode discharge with niobium injection at 0.5 s.

Fig. 3 X-ray spectra in the vicinity of the $n=2, 3$ and 4 resonance lines, w_2 (top), w_3 (middle) and w_4 (bottom), showing the $n=2$ dielectronic satellites k and j (red), and $n=2$ inner shell satellites q and r (green) and s and t (purple), along with the related higher n satellite groups A_n (red), B_n (green) and C_n (purple). The A_5 dielectronic satellite group associated with w_5 is also visible, along with two high n neon-like Mo^{32+} lines (see next section).

Fig. 4 Expanded view of the $n=4$ satellite groups of Ar^{15+} . The calculated individual constituents of the three groups A_4 , B_4 and C_4 are shown by the thin black lines with each composite depicted by the thick red, green and purple lines, respectively, for comparison with the observed spectrum in thick black.

Fig. 5 The observed x-ray spectra of Ar^{16+} w_4 with satellites, for three different central electron temperatures, are shown in black. The calculated spectra for w_4 , A_4 and A_5 are shown in red, C_4 in purple and B_4 in green.

Fig. 6 The linear scale x-ray spectrum of heliumlike Ar^{16+} w_4 , w_5 and w_6 , with satellites, and hydrogenlike Ar^{17+} $\text{Ly}\beta$, is shown in the top frame. In the bottom frame is the log scale observed spectrum (black) and the computed spectrum for Ar^{16+} (green), Ar^{17+} (purple) and Ar^{15+} (red).

Fig. 7 The difference between the satellite wavelengths and the resonance line wavelengths in Ar^{16+} as a function of n , for the three satellite groups, along with the theoretical wavelengths. The measured values for A_n , B_n and C_n are depicted as red asterisks, green triangles and purple dots, respectively. The satellite group A'_3 is shown as the orange \times . The theoretical wavelength differences are shown by the appropriately colored curves, with the calculated value for A'_3 (from RELAC) given by the orange dot. The solid lines are from MZ, while the dotted lines are from RELAC.

Fig. 8 Spectra near the Ar^{16+} series limit. In the top frame is the spectrum from a central chord view, in the middle frame is a spectrum from an identical plasma with a view 18.5 cm above the midplane ($r/a=.67$) and in the bottom frame is a spectrum from a similar plasma with a view 19.7 cm below the midplane ($r/a=.62$). The ionization limit is shown as the vertical line. The lower spectrum was cut off below 2990 mÅ.

Fig. 9 The Kr^{26+} 2 – 3 spectrum with satellites (composite over several similar discharges) is shown in the top frame, including the neon-like transition designations. In the bottom frame is a synthetic spectrum with neon-like krypton shown by the solid black line, fluorine-like by the purple line, sodium-like by the red line and magnesium-like by the green line.

Fig. 10 Linear and log spectra in the vicinity of 4D in Mo^{32+} are shown in the top frame. Also shown is the synthetic collisional radiative synthetic spectrum, with Ne-like lines shown in black, Na-like transitions depicted by the red dotted lines, the Mg-like transition shown as the green dashed line and F-like transitions shown by purple dash-dot lines. The spectrum of the Kr^{26+} 4C, 4D and 4F transitions, with Na- and Mg-like $2p_- - 4d_-$ satellites is shown in the bottom frame. Also shown is the synthetic spectrum, with Ne-like lines shown in black, Na-like transitions depicted by the red dotted lines and the Mg-like $2p_- - 4d_-$ transition shown as

the green dashed line.

Fig. 11 Measured (symbols) and calculated (lines) x-ray brightness profiles using the charge state density profiles of Fig. 4a of Ref.[48] are shown in the top frame. The solid lines are from Ne-like molybdenum, red dotted lines from Na-like and purple dashed lines from F-like. Calculated brightness profiles for the ionization balance of Fig.4b in Ref.[48] are shown in the bottom.

Fig. 12 The n=4 energy level diagrams for Mo^{32+} (top) and Kr^{26+} (bottom) with the left ordinates expressed in the transition (to the ground state) wavelengths and the right ordinates in eV. Upper levels for s and d are on the left in green and on the right in red. Measured transition wavelengths (to the ground state) are given for each of the upper levels.

Fig. 13 Calculated oscillator strengths (top) of 2p-6d and 2p-7d transitions and calculated wavelength differences (bottom) between 6C transitions and 7D transitions as a function of atomic number Z.

Fig. 14 The intensity ratios of Ne-like 7D to 6C transitions as a function of energy level separation. Calculations are shown as green dots, measurements are represented as red asterisks.

Fig. 15 Transitions in Mo^{32+} near the $2p_{\frac{3}{2}} - nd_{\frac{5}{2}}$ series limit, including the $2p_{\frac{1}{2}} - nd_{\frac{3}{2}}$ series (green) with $8 \leq n \leq 13$ and the $2p_{\frac{3}{2}} - nd_{\frac{5}{2}}$ series (red) with $11 \leq n \leq 18$. Theoretical lines for Mo^{32+} (solid red, green and purple), Mo^{33+} (black dashed), and Ar^{17+} (purple dotted) are shown at the bottom.

Fig. 16 Transitions in Mo^{32+} near the $2p_{\frac{1}{2}} - nd_{\frac{3}{2}}$ series limit for (top) $T_e = 3400$ eV and (bottom) $T_e = 2100$ eV. Theoretical lines for Mo^{32+} (solid) and Mo^{33+} (dashed) are shown at the bottom, and the vertical dashed lines indicate the series limits.

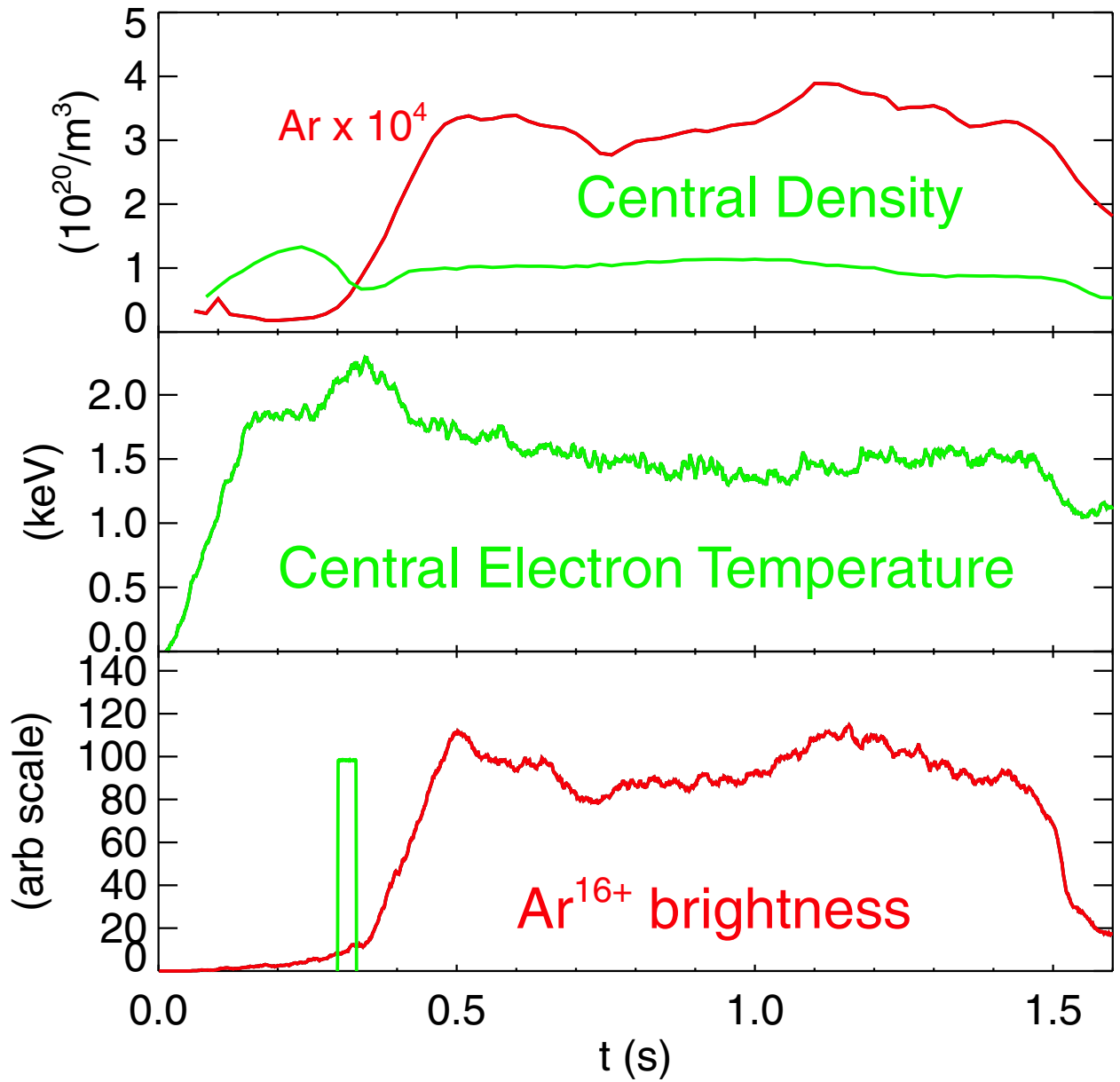


Figure 1

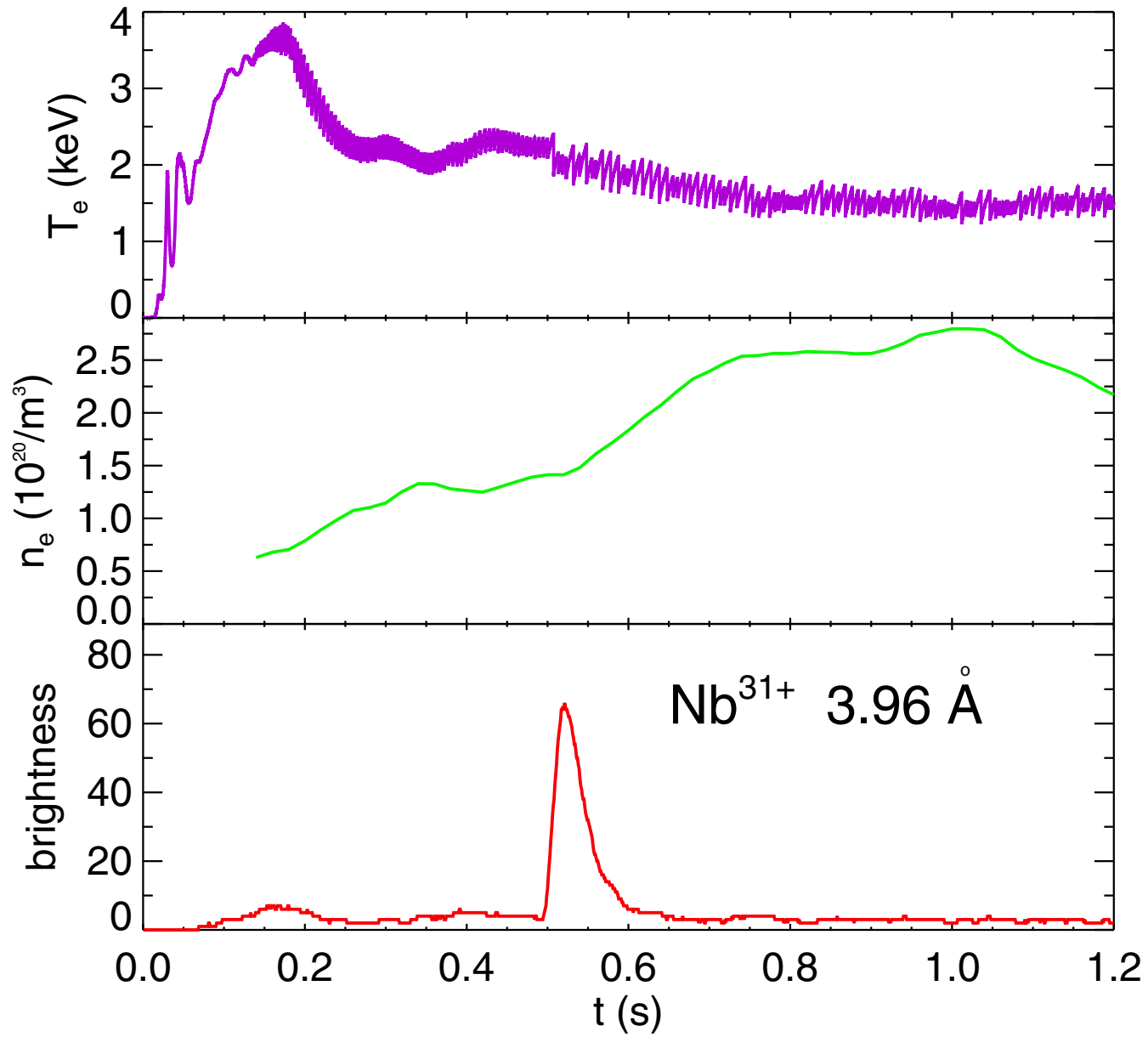


Figure 2

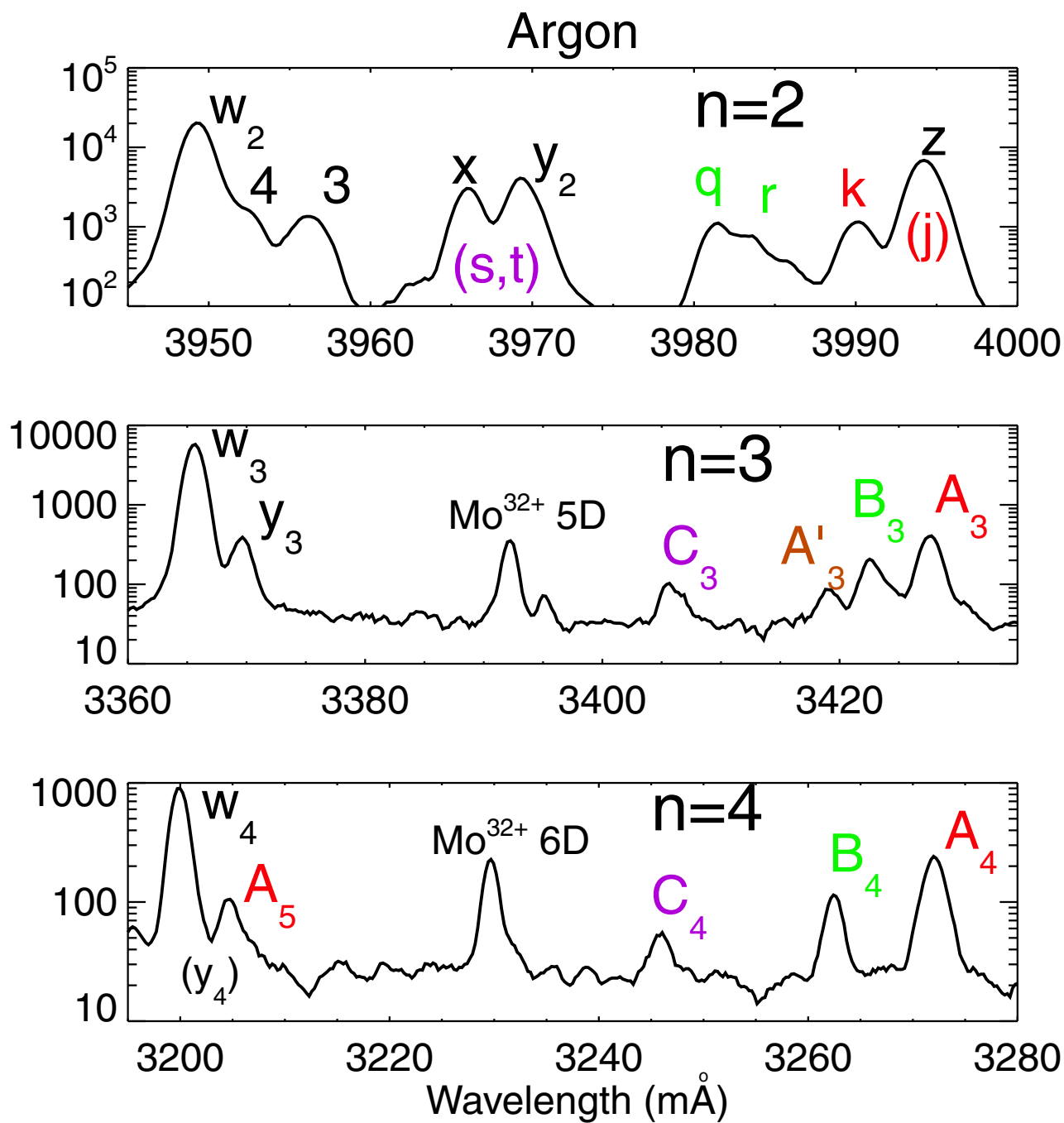


Figure 3

Ar¹⁵⁺

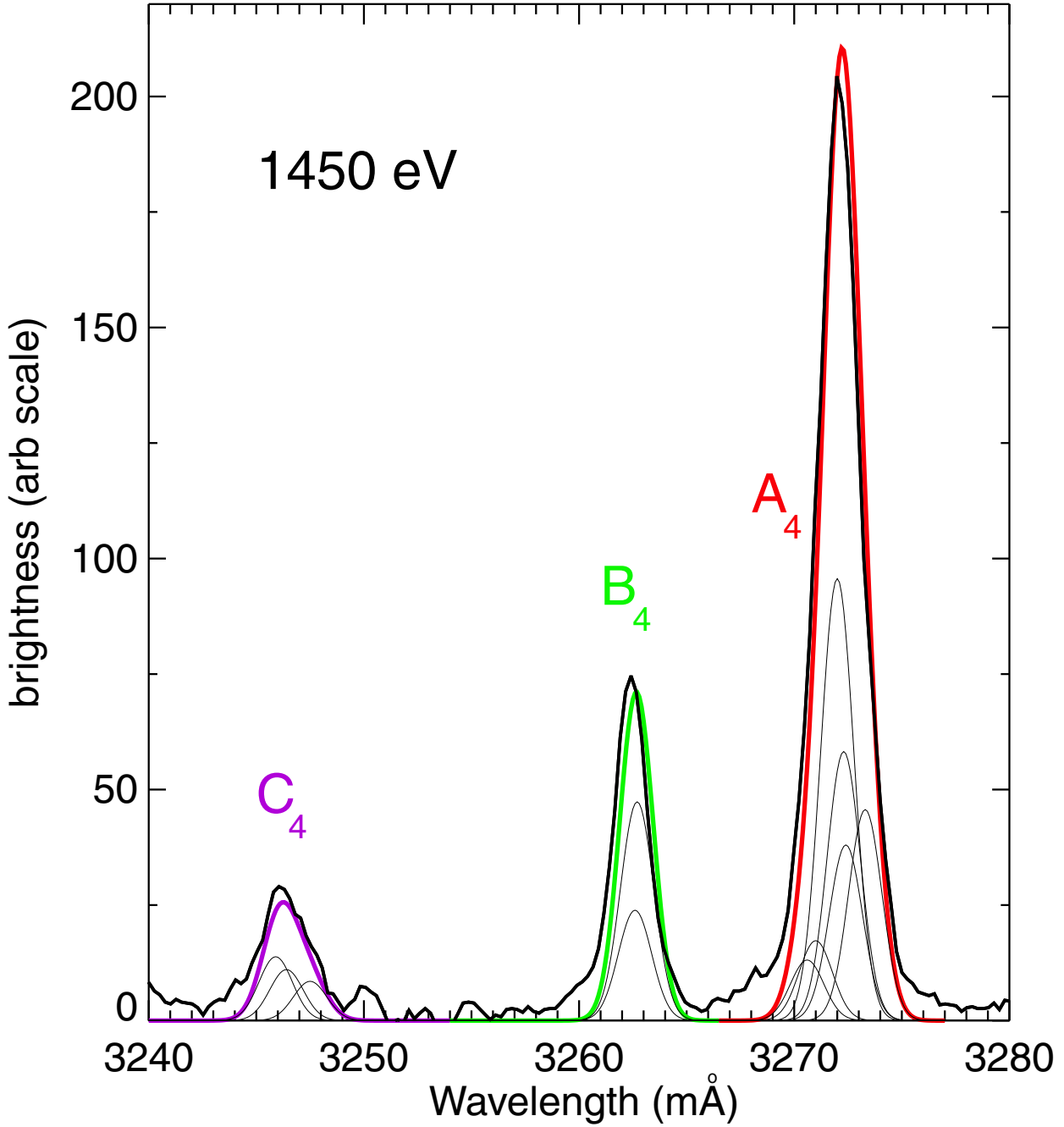


Figure 4

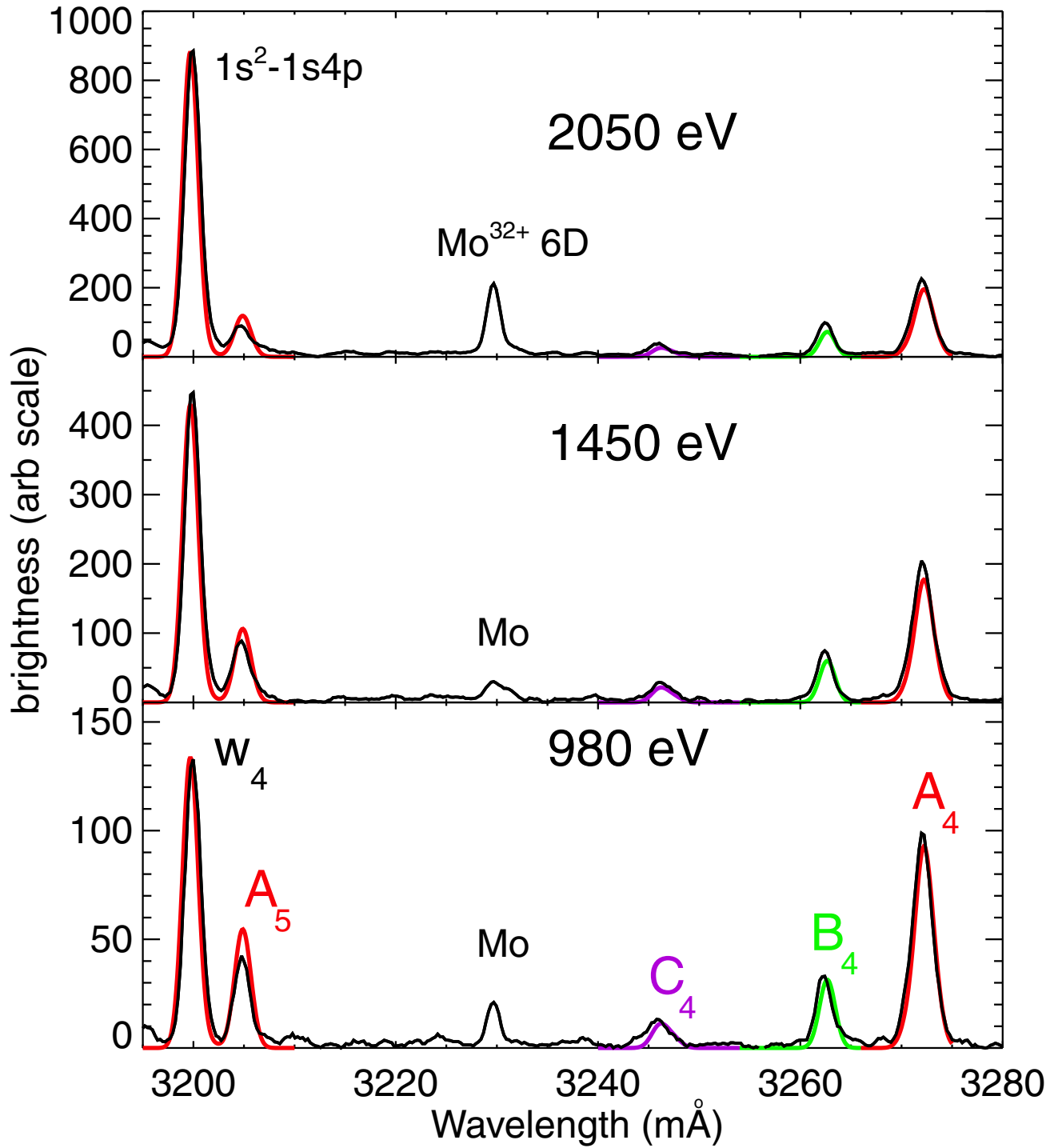
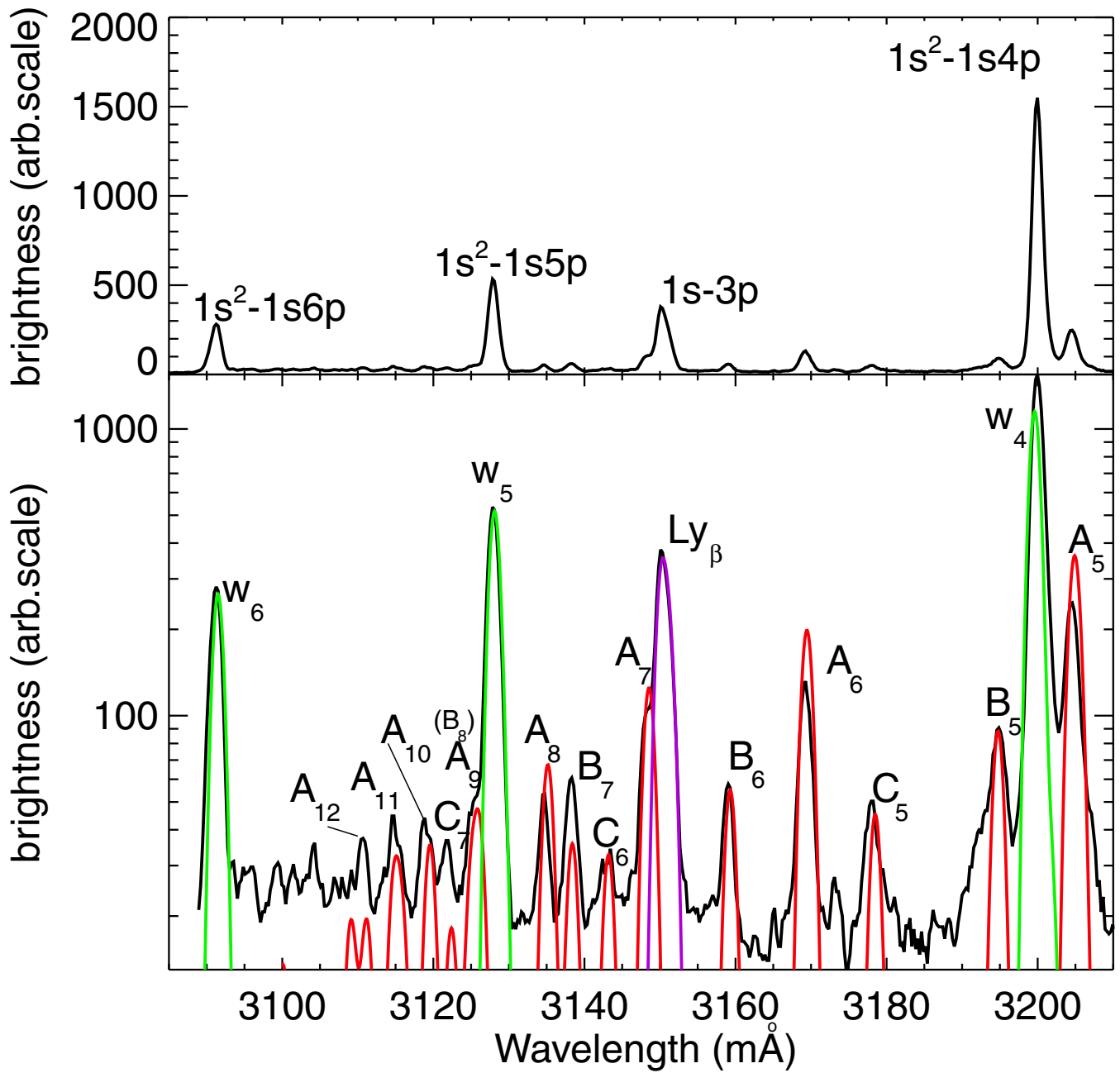


Figure 5



Ar¹⁵⁺

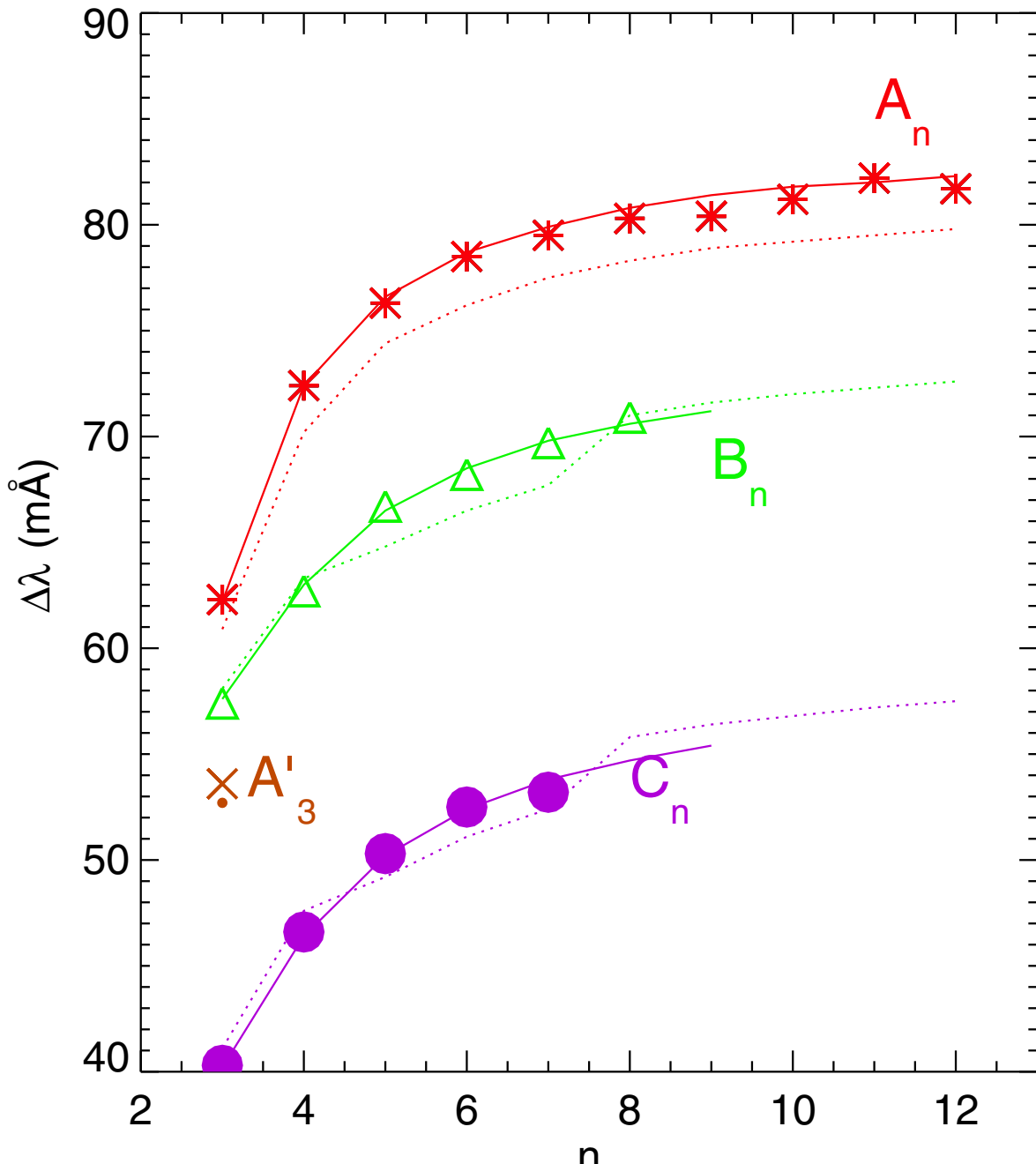


Figure 7

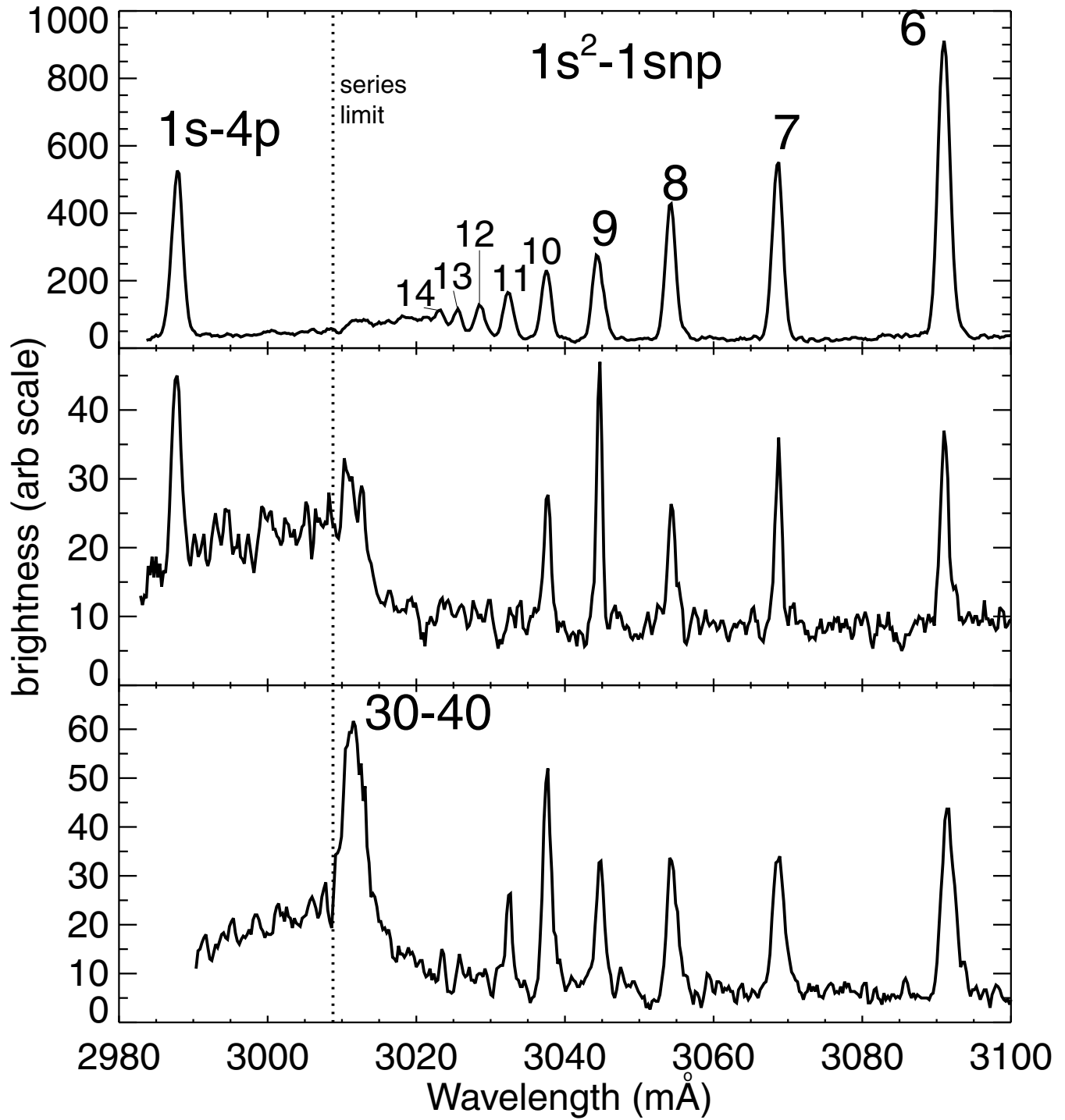


Figure 8

2-3 Kr²⁶⁺ and Satellites

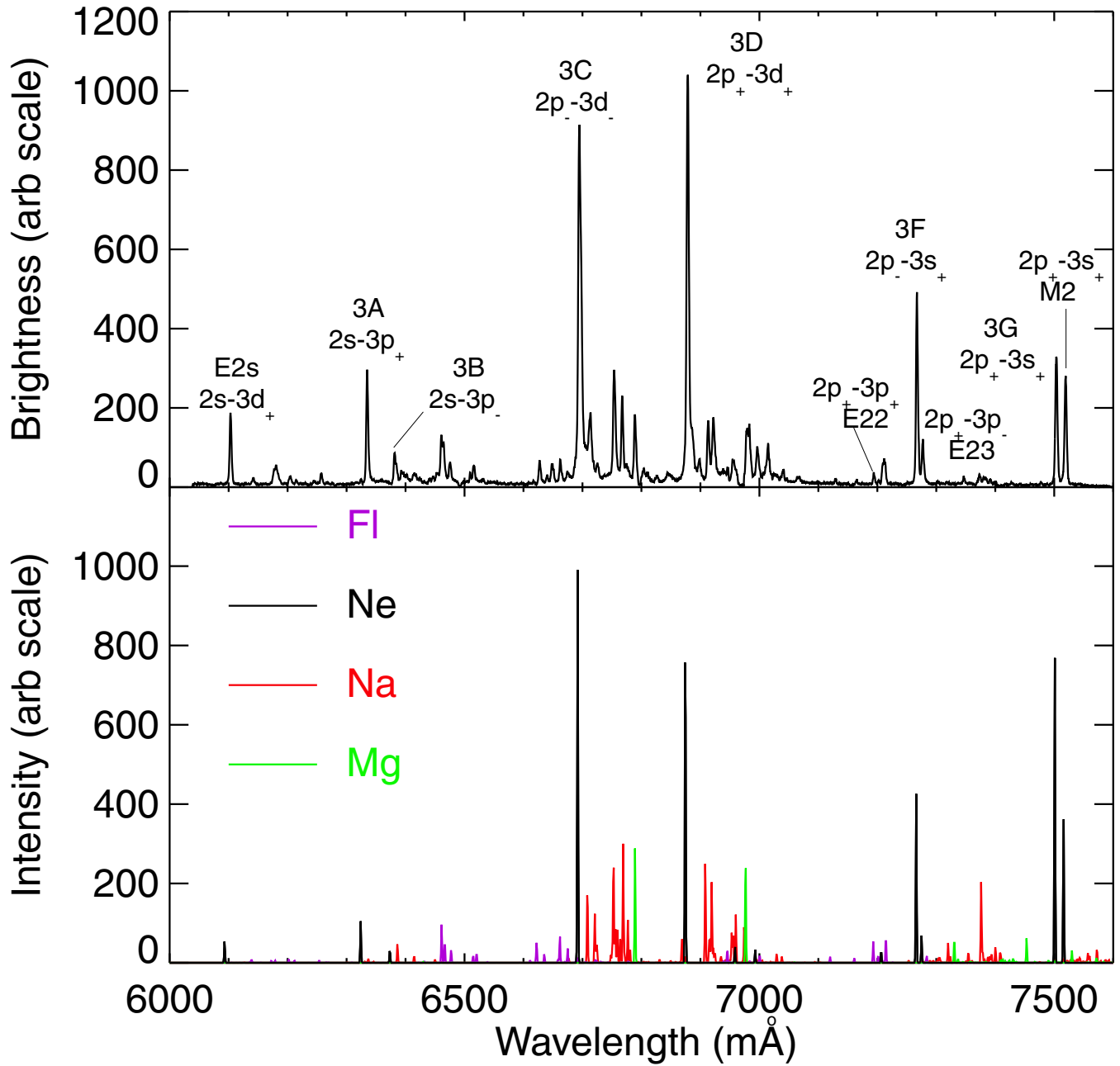


Figure 9

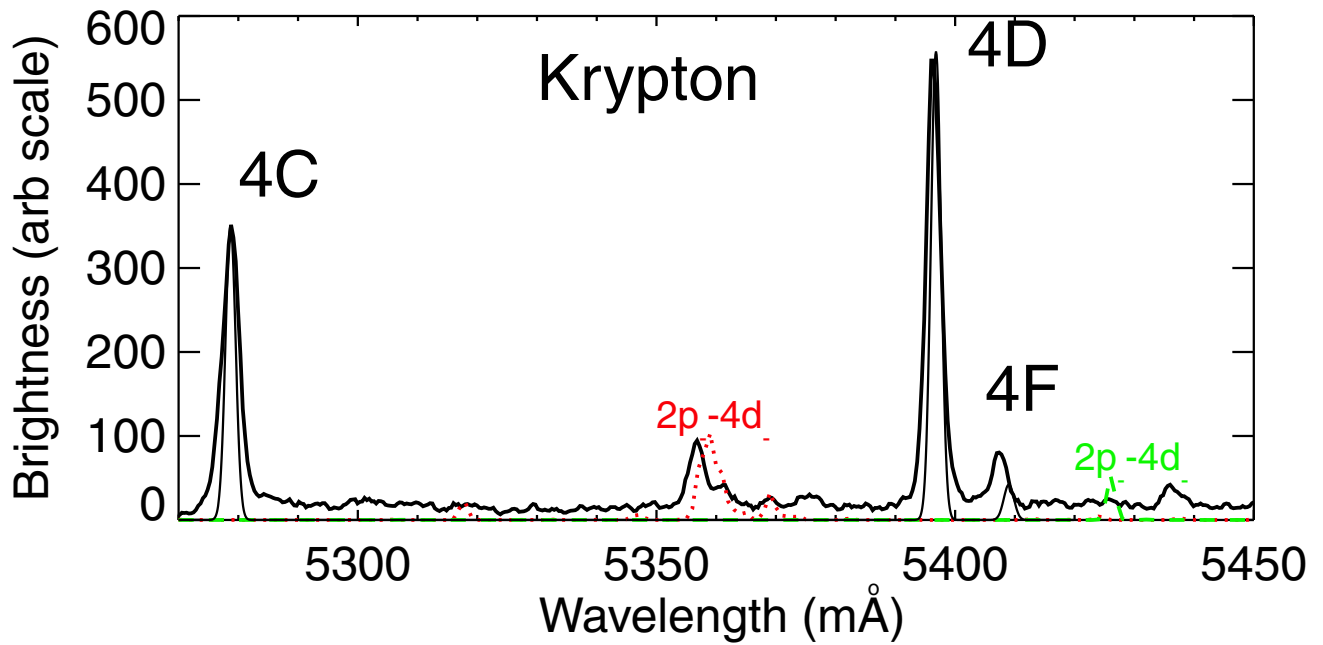
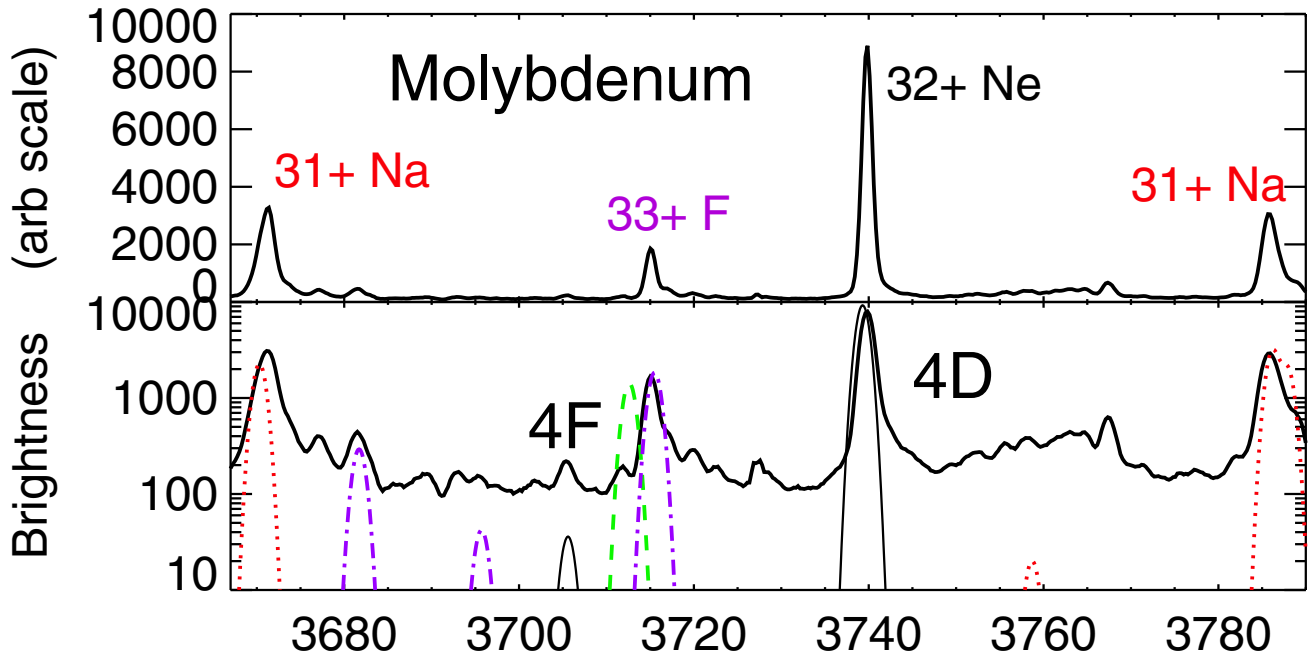


Figure 10

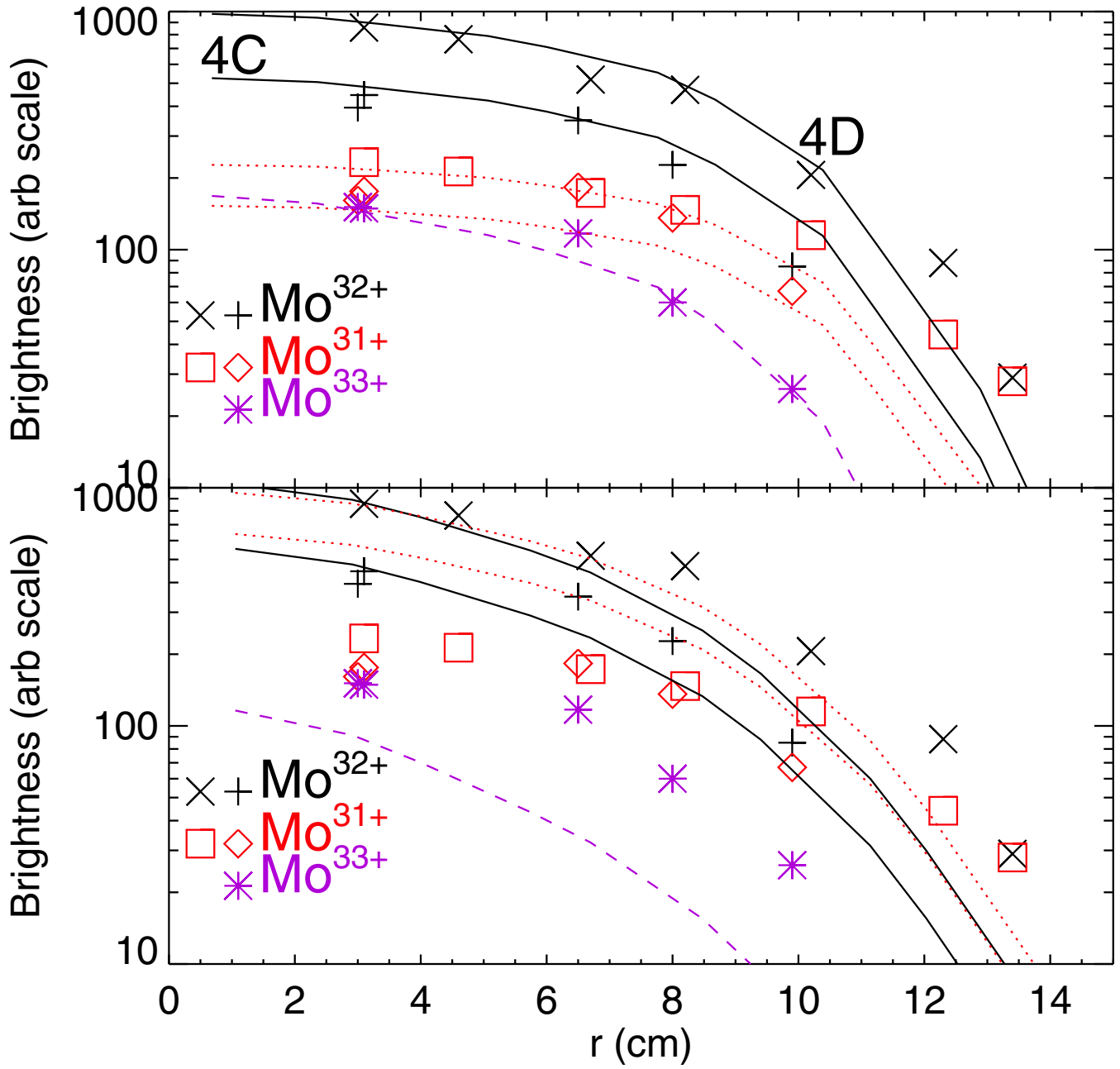


Figure 11

Neon-like Energy Levels

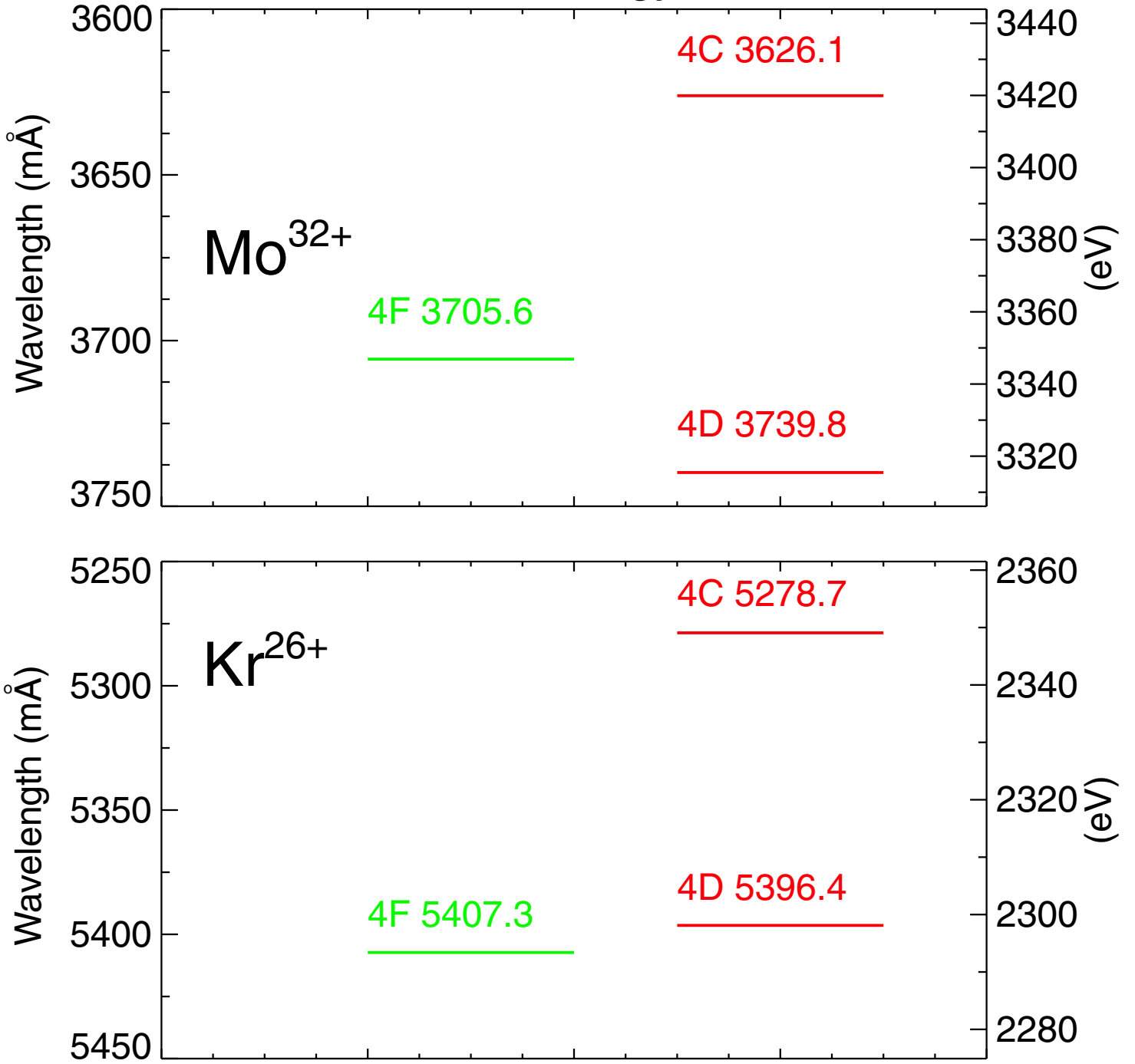


Figure 12

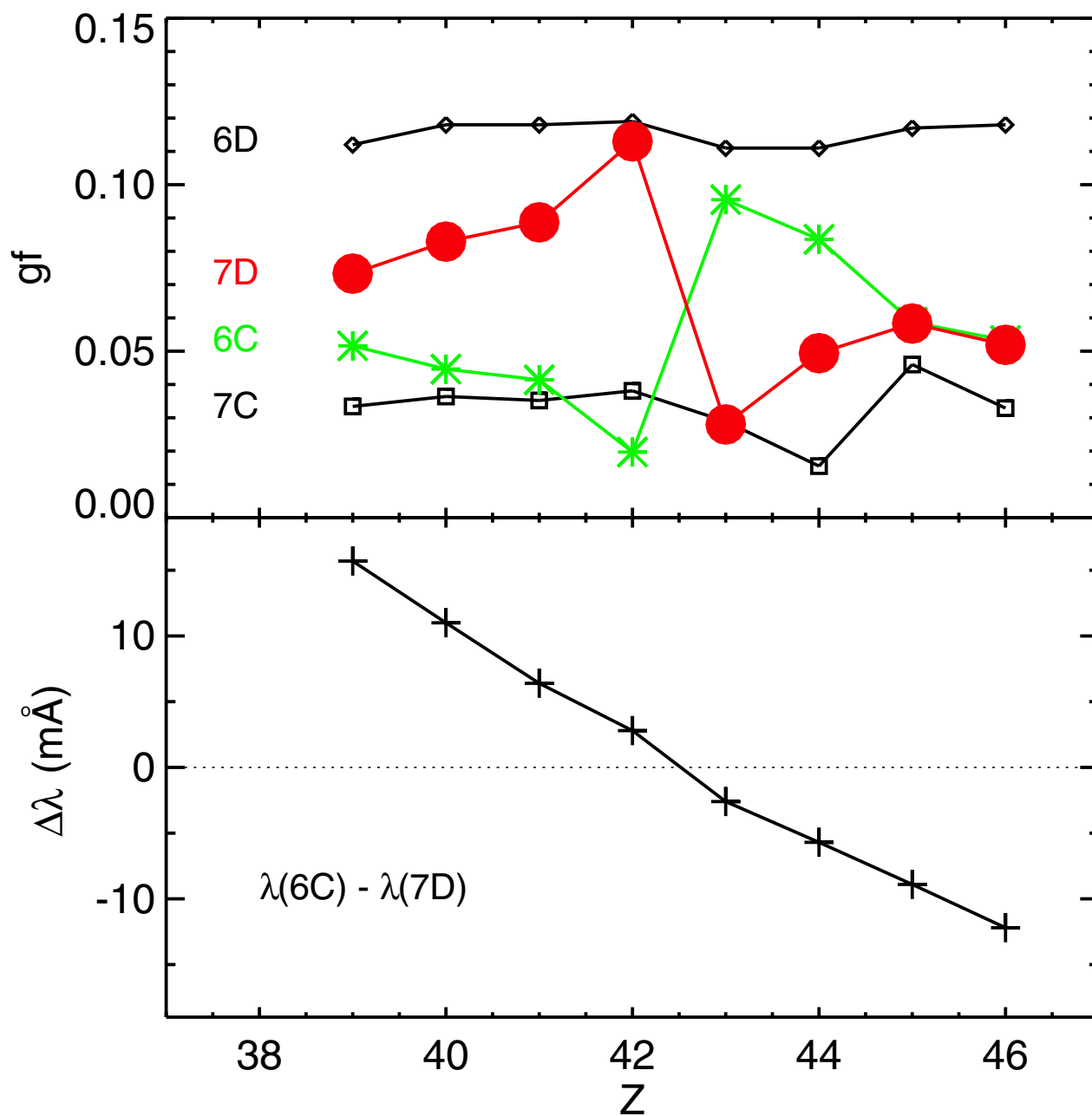


Figure 13

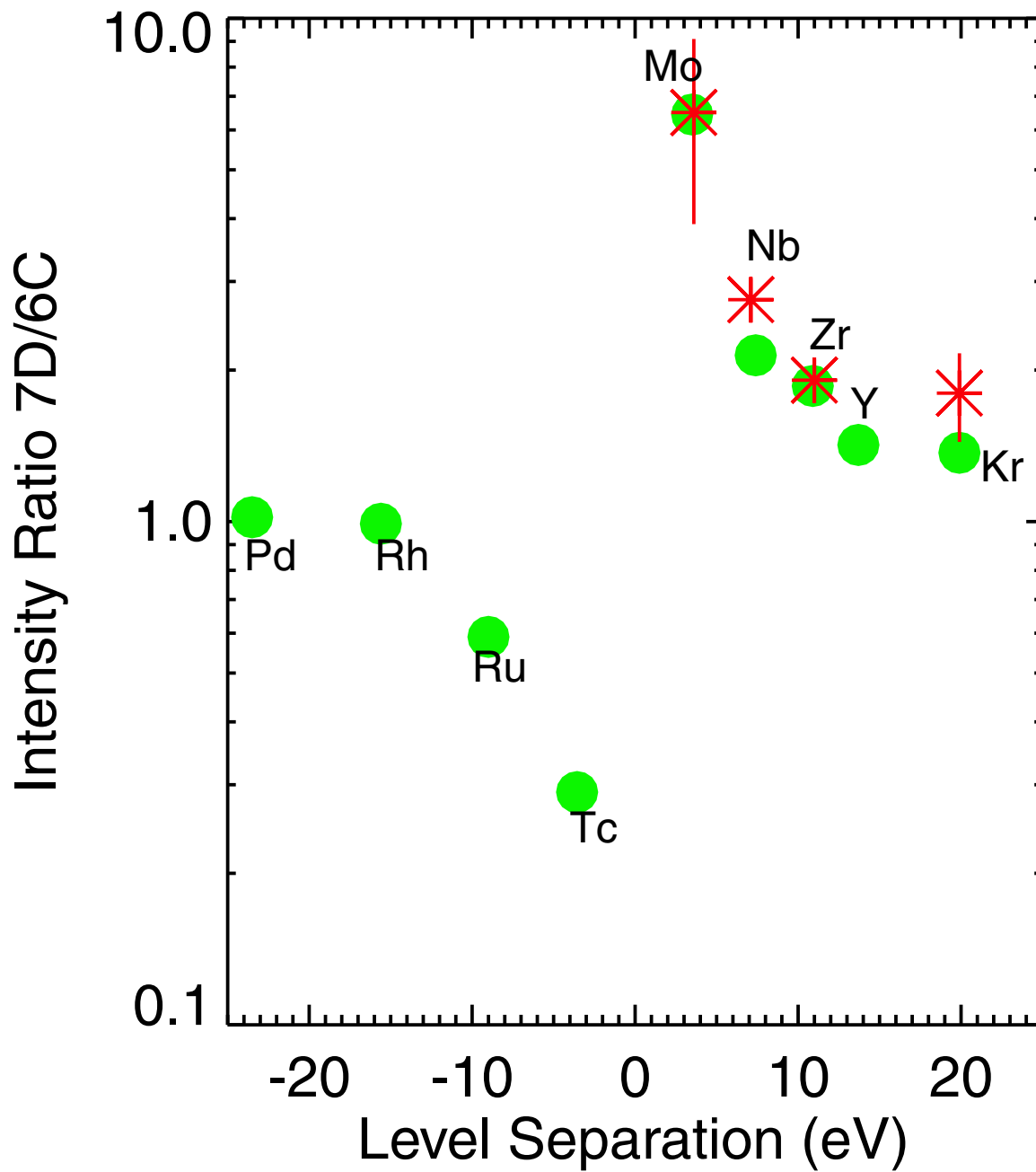


Figure 14

Mo³²⁺ 2p-nd Rydberg Series

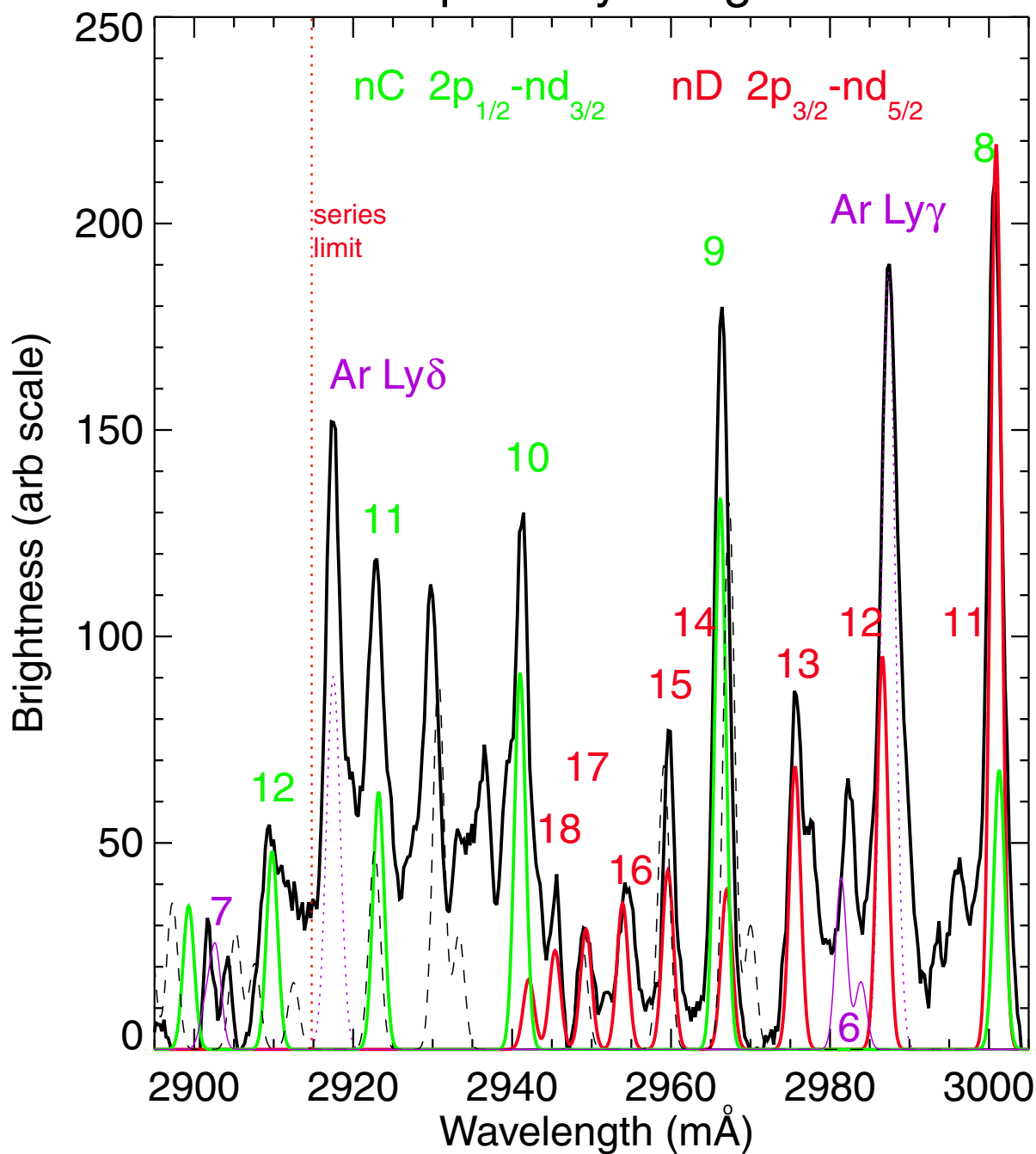


Figure 15

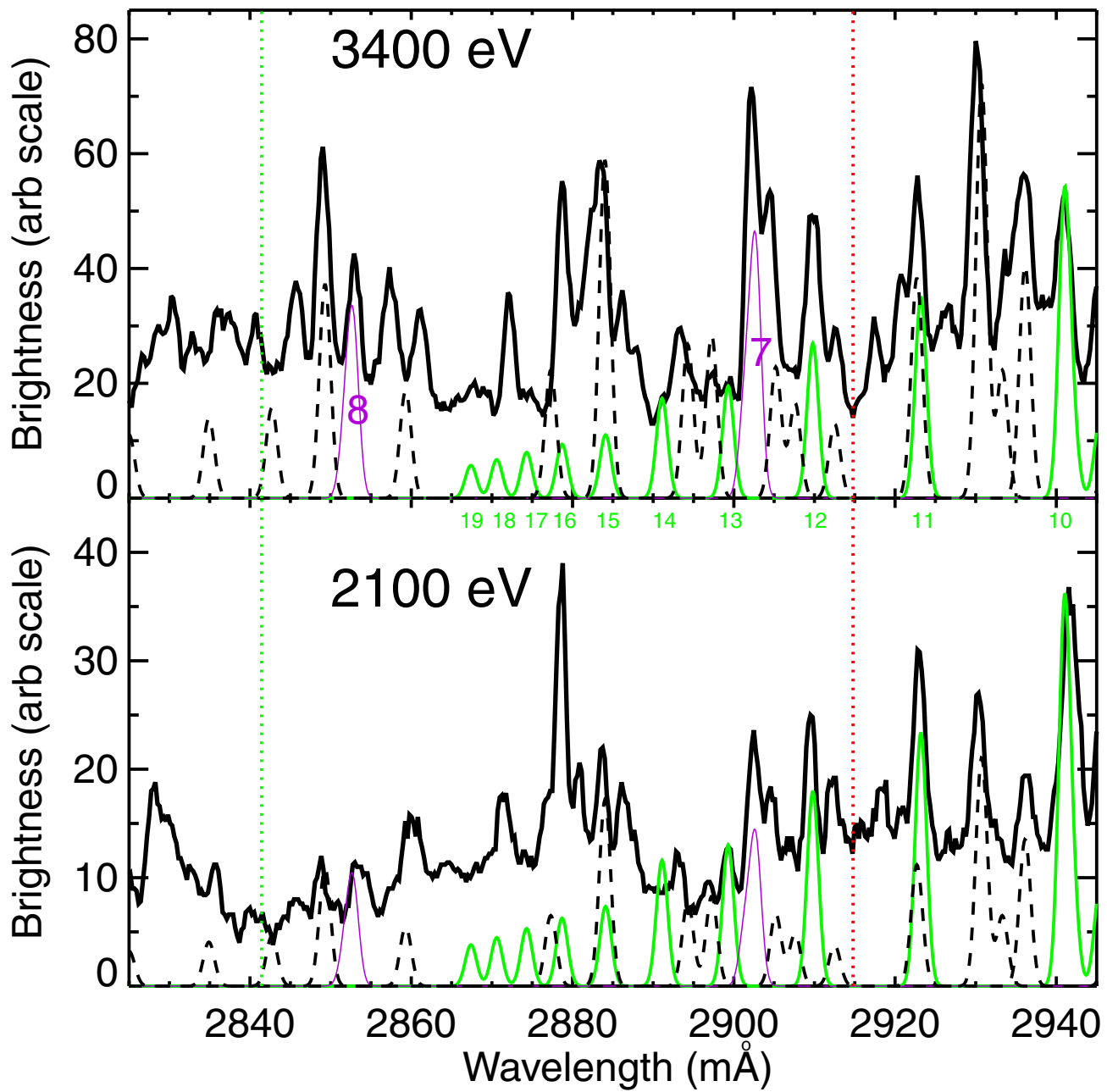


Figure 16